electronics

Article

An Active Clamp Dual-Inductor Isolated Current Source to Current Source Converter with Wide Output Voltage Range

Tiesheng Yan [1,*], Wenyuan Chen [1], Yu Zhou [1], Dong Lin [1], Jun Tian [2] and Guohua Zhou [3]

[1] School of Electrical Engineering and Electronic Information, Xihua University, Chengdu 610039, China
[2] PowerChina Sichuan Electric Power Engineering Co., Ltd., Chengdu 610041, China
[3] School of Electrical Engineering, Southwest Jiaotong University, Chengdu 611756, China
* Correspondence: tieshengyan@mail.xhu.edu.cn

Abstract: Human observation of the ocean has gradually evolved from the sea surface to systematic monitoring and sampling through seafloor observation networks, and constant current power supply has become the main power supply method for seafloor observation networks due to its high reliability. There are some studies on current source to voltage source converters, but there are few studies on current source to current source (CS/CS) converters, which affects the expansion of power supply networks for seafloor observation networks. In this paper, by employing input current sharing and output voltage doubling circuits, an active clamp dual-inductor isolated CS/CS converter which uses a single-stage conversion circuit to realize constant current source conversion with a wide output voltage range is proposed. Active clamp technology at the primary side of the proposed circuit is employed to recover energy stored in leakage inductance, suppress voltage spikes of the primary side switches, and achieve zero-voltage switching of the primary side switches. The secondary side's output voltage doubling circuit resonates with transformer leakage inductance to achieve zero-current switching of the secondary side diodes, which can reduce losses and enhance efficiency. The operating principles of the proposed circuit are analyzed in detail, and the characteristic and parameter design analysis, including current conversion ratio, transformer turn ratio, power inductors, and resonant capacitors and inductor, are presented. Finally, the experimental results based on a 100 W experimental prototype validate the feasibility of the proposed converter.

Keywords: power supply for seafloor observation networks; current source to current source converter; active clamp; dual-inductor isolated converter

Citation: Yan, T.; Chen, W.; Zhou, Y.; Lin, D.; Tian, J.; Zhou, G. An Active Clamp Dual-Inductor Isolated Current Source to Current Source Converter with Wide Output Voltage Range. *Electronics* **2024**, *13*, 2925. https://doi.org/10.3390/electronics13152925

Academic Editor: Salvador Alepuz

Received: 16 June 2024
Revised: 17 July 2024
Accepted: 22 July 2024
Published: 24 July 2024

Copyright: © 2024 by the authors. Licensee MDPI, Basel, Switzerland. This article is an open access article distributed under the terms and conditions of the Creative Commons Attribution (CC BY) license (https://creativecommons.org/licenses/by/4.0/).

1. Introduction

Oceans play a crucial role in maintaining biodiversity, providing economic resources, and human evolution. The vast waters of the ocean provide a regulatory role for the global climate system. At the same time, marine organisms in marine ecosystems participate in complex ecological cycles, affecting key ecological processes such as the global carbon and oxygen cycles. In addition, the oceans are rich in mineral and biological resources, such as oil, natural gas, metallic minerals, and fish. These resources are of great significance for human economic development and social progress. Therefore, ocean observation techniques and equipment are also constantly evolving. Observation methods for the ocean have extended from traditional surface observation to seabed observation [1–5]. As early as the early 1970s, countries around the world had begun researching underwater observation networks. Some of the well-known ocean observation systems around the world include the Martha's Vineyard Coastal Observatory in Massachusetts, USA, the Hawaii-2 Observatory in Hawaii, the Monterey Accelerated Research System in California, the North-East Pacific Time-series Undersea Networked Experiments in Canada, the Advanced Real-Time Earth Monitoring Network in the Area in Japan, and the development of the Dense Ocean-floor Network System for Earthquakes and Tsunamis [6–10].

The power supply method with a direct current (DC) input constant current source exhibits high reliability and high efficiency, which is crucial for the long-term stable operation of underwater observation equipment [11]. In addition, even if a short circuit fault occurs in seawater, a constant current power supply can also supply the current on the fault-free cables to the load next to the fault point through an energy splitter, achieving continuous power supply to the system [12–14]. Therefore, constant current power supply is a reasonable and widely used method for the power supply of submarine observation networks with high reliability requirements [15].

A block diagram of the power supply structure of the common submarine observation networks powered by a constant current source is shown as Figure 1. The submarine observation network has a large span and is mainly composed of power feeding equipment (PFE), power branching units (PBUs), and observation nodes [16]. Among these, the shore-based high-voltage power supply equipment PFE outputs constant current electrical energy to underwater equipment. Usually, the power supply in an observation node which is connected in series with the PFE uses a current source to voltage source converter to provide electrical energy for the equipment in the observation node. Each PBU receives electrical energy from the PFE and extends electrical energy to other observation nodes which are not connected to the PFE. Due to the use of a constant current power supply in the seabed observation network, each PBU needs use a current source to current source (CS/CS) converter to provide electrical energy to the observation nodes which are not connected to the PFE; therefore, research on CS/CS converters is very necessary [17–19].

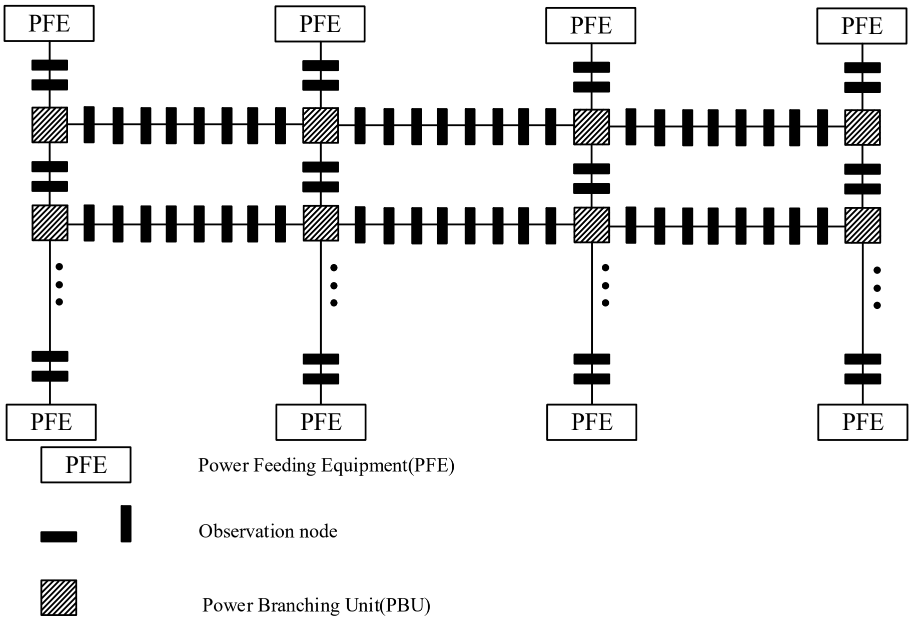

Figure 1. Block diagram of a submarine observation network.

Currently, traditional designs for converters with current source inputs employ a Zener diode matrix to convert a constant current source into a relatively stable voltage source [20]. Then, this voltage source which is generated by Zener diodes is transformed to the desired voltage for the observation equipment through an isolated DC–DC converter. When the current source flows through the Zener diode matrix, and the DC–DC converter in parallel with the Zener diode matrix, the smaller the output power of the converter, the greater the power loss of the Zener diodes, which will lead to very low efficiency and high losses with light loads. When the output load is light, it is difficult to dissipate the power consumed by the Zener diodes through natural heat dissipation, which will lead to thermal issues and reliability issues.

In [21], a basic circuit of a push–pull converter with an input inductor is proposed to achieve current source to voltage source conversion. However, this solution suffers from voltage spikes because of the leakage inductance of the transformer, and a specialized start-up and auxiliary power supply circuit need to be designed for the method. In [22], some scholars proposed a current source input converter based on full bridge resonance which adopts a single-stage circuit structure and can achieve a larger power output. The full bridge switch can achieve zero-voltage turn-on to reduce the turn-on loss of the switch and improve the efficiency of the converter. However, this converter in [22] is difficult to adapt to light-load operation and requires setting a minimum load. In [23], by using a current-fed three-phase three-leg bridge, three single-phase rectifier bridges, and three single-phase transformers with a primary star connection, a new three-phase current-fed isolated converter is presented to achieve a constant current source input, high gain, and medium power level power source. Considering its multiphase feeding design, synchronization and coordination control between different phases are crucial, and accurate control logic timing is required to adjust each switch to ensure a stable output voltage. In [24], by cascading a pre-stage push–pull current-fed circuit and a post-stage boost constant voltage converter, a two-stage isolated current source to voltage source converter for cabled underwater information networks was proposed. However, the topology uses a two-stage converter, which will affect the efficiency and power density. The topologies in [21–24] feature converters which convert current source to voltage source, but these converters cannot be used in PBUs because they cannot provide constant current source output. In [5,25], the scholars used push–pull topology to achieve a CS/CS converter where the output current's average magnitude is proportional to the input current's average magnitude, but the output current value cannot be regulated to a constant value because of the absence of closed-loop control. This converter can realize an output current source with a wide output range, but the efficiency of the converter is not high, especially with low output power, because of the hard switch.

By employing input current sharing and output voltage doubling circuits, an active clamp dual-inductor isolated CS/CS converter which uses a single-stage conversion circuit to realize constant current source conversion with a wide output voltage range is proposed in this paper. To enhance efficiency, active clamp technology at the primary side of the proposed circuit is employed to recover energy stored in leakage inductance, suppress voltage spikes of the primary side switches, and achieve zero-voltage switching of the primary side switches; the secondary side's output voltage doubling circuit resonates with the transformer leakage inductance to achieve zero-current switching of the secondary side diodes. The operating principles and the parameter design analysis of the proposed circuit, including the power inductors, transformer, and resonant capacitors, are analyzed in detail. The experimental results based on a 100 W experimental prototype validate the feasibility of the proposed converter, and the efficiency of the converter, with rated output power, can reach 91.6%.

This paper consists of five sections, as follows. The operating principle of the proposed active clamp dual-inductor isolated CS/CS converter is analyzed in Section 2. The characteristic and parameter design analysis, including the current conversion ratio, transformer turn ratio, power inductors, and resonant capacitors and inductor, are presented in Section 3. Verification results based on a 100 W experimental prototype are given to verify the feasibility of the proposed converter in Section 4. A summary of the conclusions is provided in Section 5.

2. Operating Principle of Active Clamp Dual-Inductor Isolated CS/CS Converter

2.1. Operating Principle of Main Circuit Topology and Control Circuit

The main circuit and control circuit block diagram of the proposed active clamped dual-inductor isolated CS/CS converter with a wide output voltage range is shown in Figure 2.

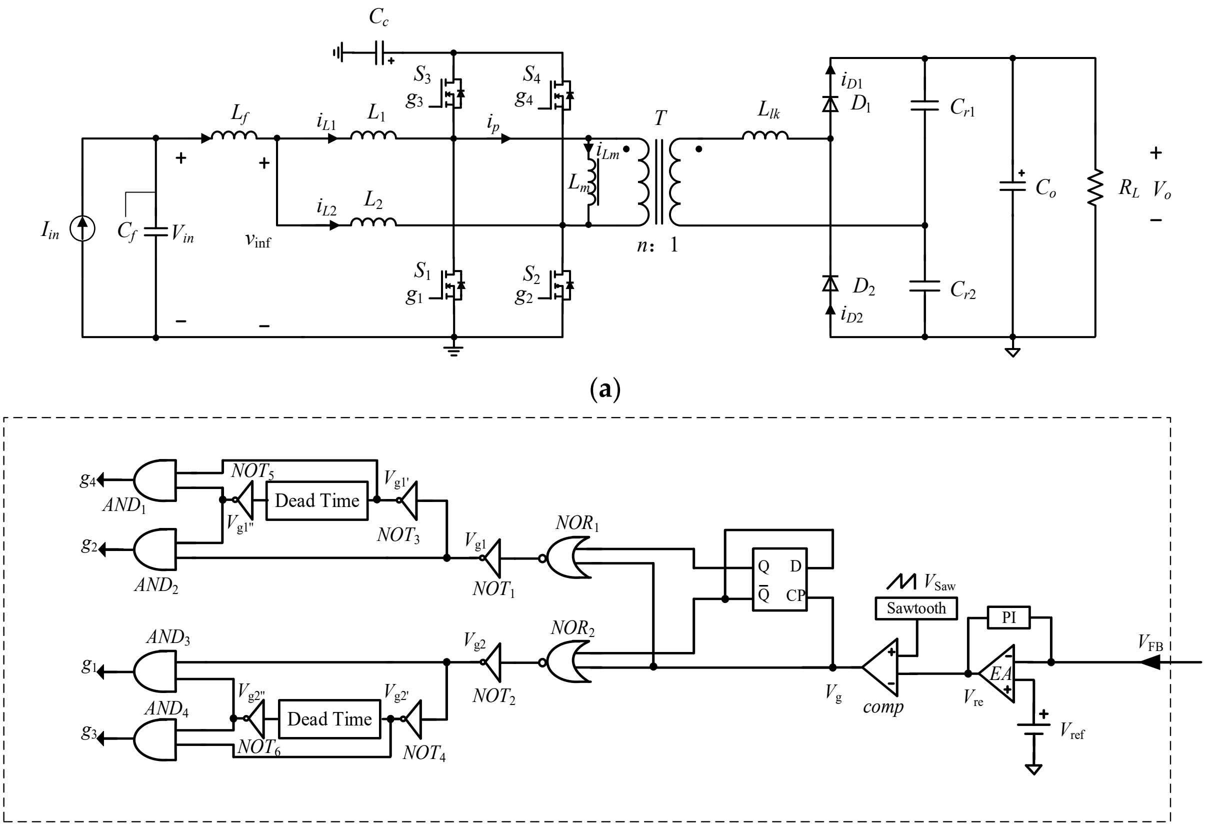

(**a**)

(**b**)

Figure 2. Main circuit and control circuit block diagram of the proposed active clamped dual-inductor isolated CS/CS converter. (**a**) Main circuit topology; (**b**) Control circuit.

As shown in Figure 2a, the proposed circuit consists of the input filter capacitor C_f, input filter inductor L_f, power inductors L_1 and L_2, clamp capacitor C_c, power switches S_1, S_2, S_3, and S_4, transformer T, secondary rectifier diodes D_1 and D_2, resonant capacitors C_{r1} and C_{r2}, resonant inductor L_{lk}, which is the secondary leakage inductance of the transformer T, and the output filter capacitor C_o. The active clamp circuit is employed on the primary side of the converter to suppress voltage spikes and return the energy stored in the leakage inductance of the transformer. The secondary output voltage doubling circuits can expand the output voltage range; as the capacitors of the voltage doubling circuit are resonant with the leakage inductance of the transformer T to improve efficiency, the proposed converter can achieve a wide output voltage range.

The control circuit block diagram of the proposed converter is shown in Figure 2b. The control circuit of the converter consists of the error amplifier EA, PI compensation circuit, comparator *comp*, sawtooth wave generator *Sawtooh*, D Flip-Flop, NOR gates NOR_1 and NOR_2, NOT gates NOT_1, NOT_2, NOT_3, NOT_4, NOT_5, and NOT_6, and AND gates AND_1, AND_2, AND_3, and AND_4. By sampling the output current and converting it into a voltage signal V_{FB} for feedback to the control system, V_{FB} is compared with the reference voltage V_{ref} to generate an error signal. The duty cycle signal V_{g} is obtained by comparing the sawtooth wave V_{saw} and error signal. Since the input power source is a current source, the duty cycle of the main switches S_1 and S_2 should be greater than 0.5, ensuring that the proposed converter always has a continuous current path from the current source to the ground. The PWM driving signals of the active clamp switches S_4 and S_3 are 180° out of phase from the driver signal of the main switches S_1 and S_2.

For the convenience of theoretical analysis, it is assumed that all switches, diodes, inductors, and capacitors in the topology are ideal components. There are ten operating modes within one switching cycle of the proposed converter. Since the proposed converter can operate symmetrically, only the five operation modes during the first half of the switching cycle are analyzed. Figures 3 and 4 illustrate the operation modes and key waveforms of the proposed topology.

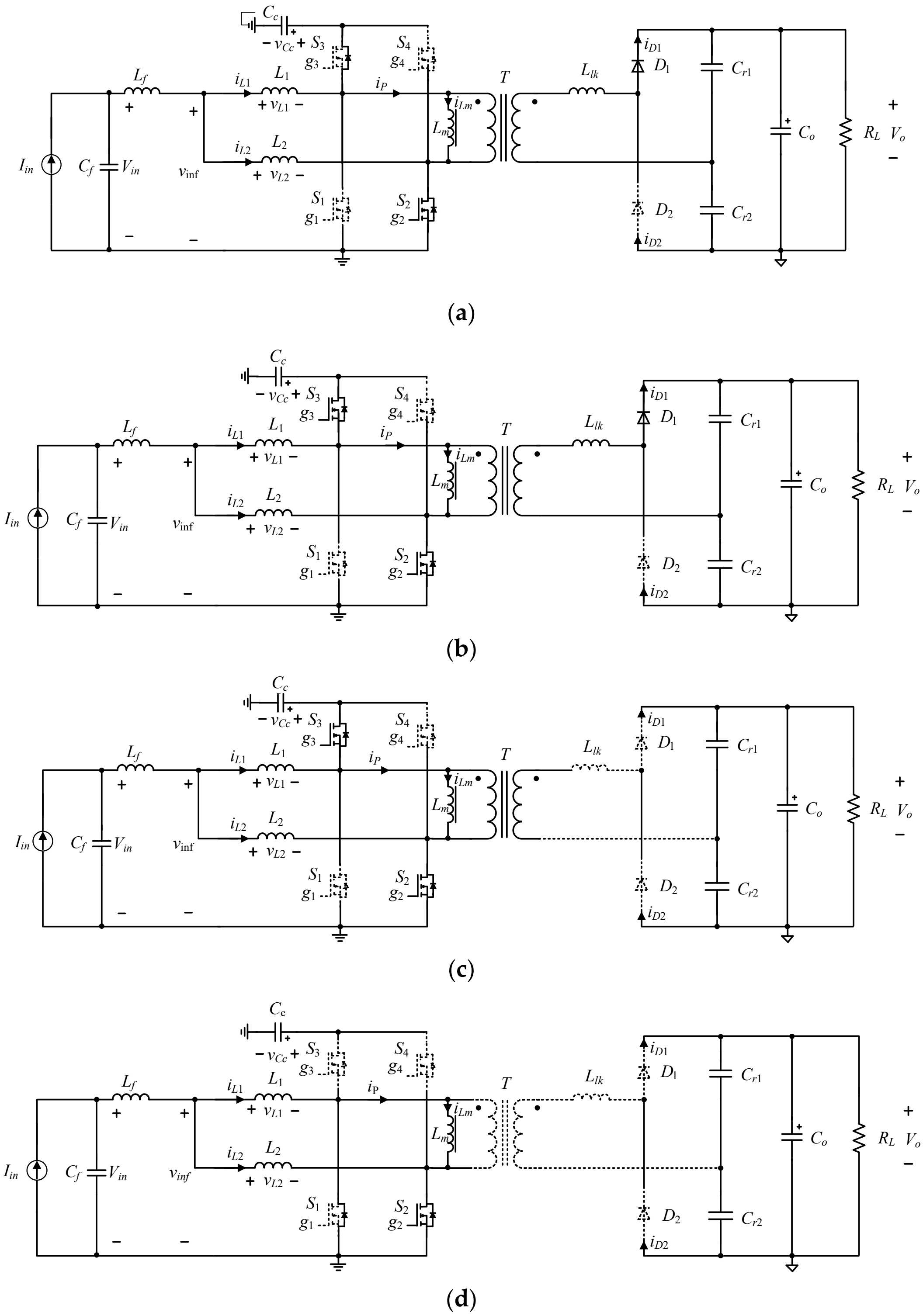

(**a**)

(**b**)

(**c**)

(**d**)

Figure 3. *Cont.*

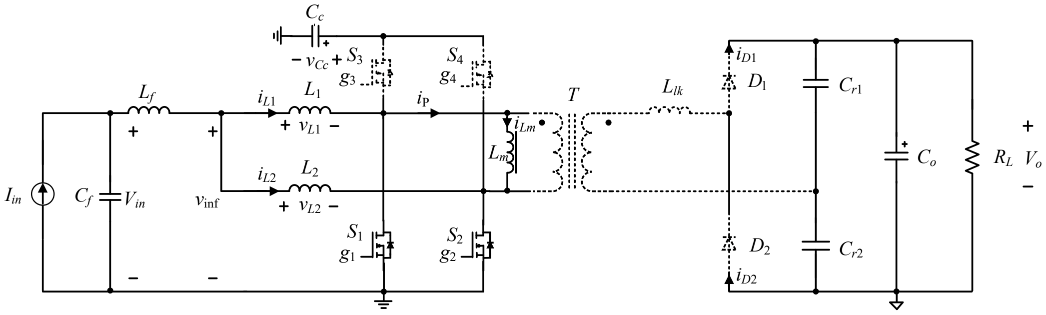

(e)

Figure 3. Operation modes during the first half of the switching cycle. (**a**) Mode A; (**b**) Mode B; (**c**) Mode C; (**d**) Mode D; (**e**) Mode E.

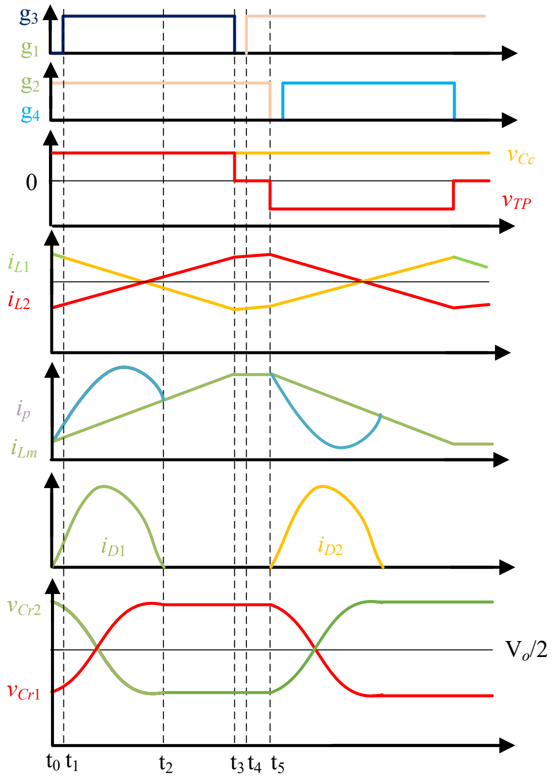

Figure 4. Main waveforms of the proposed topology.

2.2. Operation Modes Analysis

Mode A ($t_0 - t_1$): As shown in Figure 3a, S_2 is turned on and S_1, S_3, and S_4 are turned off during Mode A. This mode represents a transient dead-time period. During this mode, the current i_{L1} through inductor L_1 decreases linearly, the current i_{L2} through inductor L_2 increases linearly, and the magnetic current i_{Lm} linearly increases. Concurrently, resonance occurs between the secondary side inductor L_{lk} and resonant capacitors C_{r1} and C_{r2}, causing the secondary side diode D_1 to start conducting. Since there is an imbalance between the $i_{\rm p}$ and i_{L1} currents at this point, the body diode of switch S_3 conducts. Current flows through switch S_3, resulting in zero-voltage switching for switch S_3.

Mode B ($t_1 - t_2$): As depicted in Figure 3b, S_1 and S_4 are turned off and S_2 and S_3 are turned on. During this mode, the power source charges the clamp capacitor C_c through L_1, i_{L1} decreases linearly, and the current i_{L2} through inductor L_2 increases linearly. The primary voltage v_{TP} of the transformer voltage is equal to the voltage v_{Cc} across the clamp capacitor C_c.

The secondary side inductor L_{lk} and resonant capacitors C_{r1} and C_{r2} remain in resonance. The secondary side diode D_1 conducts, causing the voltage across C_{r1} to rise and the voltage across C_{r2} to fall. Energy is transferred from the primary side to the secondary side until diode D_1 turns off in this mode.

During this interval, the voltages v_{L1} and v_{L2} across inductors L_1 and L_2 are shown as

$$v_{L1} = v_{\text{inf}} - v_{Cc} = -L_1 \frac{\Delta i_{L1}}{\Delta t} \tag{1}$$

$$v_{L2} = v_{\text{inf}} = L_2 \frac{\Delta i_{L2}}{\Delta t} \tag{2}$$

where v_{inf} is the input voltage after inductor L_{f}, and Δi_{L1} and Δi_{L2} are the variation of the inductor currents i_{L1} and i_{L2}, respectively.

In Mode B, the currents through inductors L_1 and L_2 and the magnetic inductor L_m can be expressed as

$$i_{L1}(t) = i_{L1}(t_1) + \frac{v_{\text{inf}} - v_{Cc}}{L_1}(t - t_1) \tag{3}$$

$$i_{L2}(t) = i_{L2}(t_1) + \frac{v_{\text{inf}}}{L_2}(t - t_1) \tag{4}$$

$$i_{Lm}(t) = i_{Lm}(t_1) + \frac{v_{Cc}}{L_m}(t - t_1) \tag{5}$$

where $i_{L1}(t_1)$, $i_{L2}(t_1)$, and $i_{Lm}(t_1)$ are the initial values of the currents through inductors L_1 and L_2 and the magnetic inductor L_m at time t_1, respectively.

In this mode, the primary side voltage v_{TP} of the transformer is given as

$$v_{TP} = v_{Cc} \tag{6}$$

The secondary side voltage v_{sec} of the transformer secondary side can be expressed as

$$v_{\text{sec}} = \frac{v_{Cc}}{n} \tag{7}$$

where n is the ratio of the turn number of primary side to the turn number of the secondary side.

When the transformer's secondary side is in resonance, the related resonant current of the secondary side can be given as

$$L_{lk} \frac{di_{Lr}(t)}{dt} = -\frac{v_{Cc}}{n} + v_{cr1}(t) \tag{8}$$

$$i_{lk}(t) = C_{r1} \frac{dv_{cr1}(t)}{dt} - C_{r2} \frac{dv_{cr2}(t)}{dt} \tag{9}$$

where v_{cr1} and v_{cr2} are the voltage values across resonant capacitors C_{r1} and C_{r2}, respectively, and i_{lk} is the current through the leakage inductance of transformer T.

Supposing the resonant capacitances of both C_{r1} and C_{r2} are same, the voltage ripple of the resonant capacitor C_{r1} can be expressed as

$$\Delta v_{cr} = \frac{1}{C_r} \int_{t_1}^{t_2} i_{cr1}(t)dt = \frac{1}{2C_r} \int_{t_1}^{t_2} i_{D1}(t)dt = \frac{T_s I_o}{2C_r} \tag{10}$$

where T_s is switching period, C_r is the capacitance value of resonant capacitors C_{r1} and C_{r2}, and I_o is the output current of the proposed converter.

The initial resonance situation can be assumed as

$$i_{lk}(t_0) = 0 \tag{11}$$

$$V_{cr1}(t_0) = \frac{V_o}{2} - \frac{\Delta V_{cr}}{2} \tag{12}$$

According to Figure 3, the output voltage is the sum of the voltage resonant capacitors C_{r1} and C_{r2}, so the output voltage can be expressed as

$$V_o = V_{cr1} + V_{cr2} \tag{13}$$

From (8)–(13), the current through leakage inductance and the voltage values across resonant capacitors can be given as

$$i_{lk}(t) = \frac{V_c + nV_{cr1}(t_1)}{nZ_r} \sin[\omega_r(t - t_1)] \tag{14}$$

$$v_{cr1}(t) = \frac{V_{Cc}}{n} + (V_{cr1}(t_1) + \frac{V_{Cc}}{n}) \cos[\omega_r(t - t_1)] \tag{15}$$

where ω_r is the angular resonant frequency, Z_r is the resonant impedance, and ω_r and Z_r can be given as

$$\omega_r = \frac{1}{\sqrt{L_{lk}(C_{r1} + C_{r2})}} = \frac{1}{\sqrt{2L_{lk}C_{r1}}} \tag{16}$$

$$Z_r = \sqrt{\frac{L_{lk}}{C_{r1} + C_{r2}}} = \sqrt{\frac{L_{lk}}{2C_r}} \tag{17}$$

Mode C ($t_2 - t_3$): As shown in Figure 3c, the resonance of L_{lk}, C_{r1} and C_{r2} is ended at t_2, and the current through diode D_1 becomes zero at t_2. Zero-current turn-off of diode D_1 is achieved to eliminate the reverse recovery power loss. In this mode, switches S_1 and S_4 remain off while switches S_2 and S_3 remain on.

In this mode, the system provides energy from the output filter capacitor C_o to the load, maintaining a constant output current. The current through inductor i_{L1} continues to decrease with the same slew rate of Mode B, while i_{L2} continues to increase with the same slew rate of Mode B as well.

Therefore, the currents through inductors L_1 and L_2, and the magnetic inductor L_m in Mode C can be given as

$$i_{L1}(t) = i_{L1}(t_2) + \frac{v_{\text{inf}} - v_{Cc}}{L_1}(t - t_2) \tag{18}$$

$$i_{L2}(t) = i_{L2}(t_2) + \frac{v_{\text{inf}}}{L_2}(t - t_2) \tag{19}$$

$$i_{\text{Lm}}(t) = i_{Lm}(t_2) + \frac{v_{Cc}}{L_m}(t - t_2) \tag{20}$$

Mode D ($t_3 - t_4$): As shown in Figure 3d, this mode represents a transient dead-time interval. In this mode, switch S_2 remains on, while switches S_1, S_3, and S_4 are off. The secondary side diodes are off. Output load energy is supplied from the output filter capacitor C_o. The voltage across the primary winding of the transformer is zero, so the current i_{Lm} of the magnetic inductor remains almost constant. The body diode of switch S_1 conducts to provide the current difference between the magnetic inductor current i_{Lm} and the current i_{L1} through inductor L_1. The voltage drop across switch S_1 is reduced to zero before the turn-on driver signal is given, and zero-voltage switching for switch S_1 is achieved.

Mode E ($t_4 - t_5$): As depicted in Figure 3e, switches S_1 and S_2 are turned on, while switches S_3 and S_4 are turned off. As both main switches S_1 and S_2 are turned on, the input voltage is applied to the inductors L_1 and L_2, the currents i_{L1} and i_{L2} increase linearly, and the voltage across the primary winding of the transformer is almost zero. Then, i_{L1} and i_{L2} can be given as

$$i_{L1}(t) = i_{L1}(t_4) + \frac{v_{\text{inf}} - v_{Cc}}{L_1}(t - t_4) \tag{21}$$

$$i_{L2}(t) = i_{L2}(t_4) + \frac{v_{\text{inf}}}{L_2}(t - t_4) \tag{22}$$

3. Characteristic and Parameter Design Analysis

3.1. Current Conversion Ratio

According to the above operation mode analysis, the relationship between the average voltage values of C_{r1} and C_{r2} on the resonant capacitor and the average output voltage value can be given as

$$V_{cr1} = V_{cr2} = \frac{V_o}{2} \tag{23}$$

According to (6), (7), and (23), the average voltage of the clamp capacitor can be expressed as

$$V_{Cc} = \frac{nV_o}{2} \tag{24}$$

According to (24), it can be seen that the voltage of the clamp capacitor is only related to the turn ratio of the transformer and output voltage, and is independent of other parameters such as the input current or output current, so the voltage of the clamp capacitor does not need special control. As long as the output voltage is stable, the V_{Cc} voltage remains stable.

Based on the above operation mode analysis, for an ideal converter, the input power should be equal to the output power:

$$I_{in}V_{Cc}\frac{L_1}{L_1 + L_2}(1 - D)T_s + I_{in}V_{Cc}\frac{L_2}{L_1 + L_2}(1 - D)T_s = V_o I_o T_s \tag{25}$$

where D is the duty cycle of main power switch S_1 and S_2, and I_{in} is the input current.

According to (24) and (25), the relationship of the input current I_{in} and output current I_o can be written as

$$I_o = \frac{nI_{in}(1 - D)}{2} \tag{26}$$

3.2. Transformer Turn Ratio Design

Observing Equation (26), the design of the turn ratio of the transformer should be related to the duty cycle range, input current I_{in}, and output current I_o. Since the duty cycle D is usually bigger than 0.5, the minimum turn ratio condition can be written as

$$n \geq \frac{2I_o}{I_{in}(1 - D)} \tag{27}$$

3.3. Inductance L_1 and L_2 Design

According to Kirchhoff's law, the relationship between the currents i_{L1} and i_{L2} through inductors L_1 and L_2 and the input current I_{in} can be expressed as

$$i_{L1} + i_{L2} = I_{in} \tag{28}$$

The current ripple Δi_{L1} and Δi_{L2} of inductors L_1 and L_2 can be defined as

$$\Delta i_{L1} = i_{L1\_\text{max}} - i_{L1\_\text{min}} \tag{29}$$

$$\Delta i_{L2} = i_{L2\_\text{max}} - i_{L2\_\text{min}} \tag{30}$$

where i_{L1_max} is the maximum current on input inductor L_1, i_{L1_min} is the minimum value of the current on input inductor L_1, i_{L2_max} is the maximum current on input inductor L_2, and i_{L2_min} is the minimum value of the current on input inductor L_2.

According to the operation theory of the proposed converter, the inductor current ripples Δi_{L1} and Δi_{L2} meet the formula

$$\Delta i_{L1} = \Delta i_{L2} \tag{31}$$

According to Equations (1), (2), (18), (19) and (24), in Modes A, B, and C, the voltages v_{L1} and v_{L2} across inductors L_1 and L_2 can be obtained as

$$v_{L1} = \frac{nV_o L_1}{2(L_1 + L_2)} \tag{32}$$

$$v_{L2} = \frac{nV_o L_2}{2(L_1 + L_2)} \tag{33}$$

From Equations (28)–(33), neglecting the dead-time period, the inductor current ripples Δi_{L1} and Δi_{L2} can be obtained as

$$\Delta i_{L1} = \Delta i_{L2} = \frac{nV_o(1 - D)}{2(L_1 + L_2)f_s} \tag{34}$$

where f_s is the switching frequency of the main power switch.

Usually, the inductors L_1 and L_2 operate in continuous conduction mode, and Δi_{L1} and Δi_{L2} should be smaller than the input current. Combing Equations (26) and (34), the inductance values L_1 and L_2 need to meet the following requirements:

$$L_1 + L_2 \geq \frac{V_o I_o}{I_{in} f_s} \tag{35}$$

From Equation (35), it can be observed that the sum of inductances L_1 and L_2 depends on the output voltage V_o, output current I_o, input current I_{in}, and switching frequency f_s. Due to the symmetrical current waveforms of inductances L_1 and L_2, they play the same role in the positive and negative half cycles. Therefore, on the basis of satisfying Equation (35), L_1 and L_2 can use the same value inductor.

3.4. Design of Clamp Capacitor C_C, Resonant Capacitor C_r, Resonant Inductor L_{lk}, and Magnetic Inductor L_m

In general, the value of the clamp capacitor can affect the voltage ripple ΔV_{Cc} of the clamp capacitor. When all output load power comes from the clamp capacitor, the voltage ripple ΔV_{Cc} of the clamp capacitor C_C is at maximum. Therefore, the voltage ripple ΔV_{Cc} should meet following equation:

$$\Delta V_{Cc} \leq \frac{T_s I_o}{2nC_C} \tag{36}$$

To ensure the correct operation of the secondary resonant circuit, the resonant capacitor C_r and inductor L_{lk} should be designed to satisfy

$$\Delta v_{cr} \leq V_o \tag{37}$$

According to the Equation (10), which is the voltage ripple expression of the resonant capacitor in the operation mode analysis of Mode B, the resonant capacitor should meet

$$C_r = \frac{T_s I_o}{2\Delta v_{cr}} \geq \frac{T_s I_o}{2V_{o\_\min}} \tag{38}$$

where $V_{o\_\min}$ is the minimum output voltage.

To guarantee zero-current switching turn-off for the rectifier diodes D_3 and D_4, the half-period π/ω_r of the resonant circuit should be less than $(1 - D)T_s$. The resonant inductance, which is also the secondary side leakage inductance of the transformer T, should meet following equation:

$$\frac{\pi}{\omega_r} = \pi\sqrt{2L_{lk}C_r} \leq (1 - D)T_s \tag{39}$$

According to (26), Equation (39) can be rewritten as

$$L_{lk} \leq \frac{8}{C_r}\left(\frac{I_o T_s}{\pi n I_{in}}\right)^2 \tag{40}$$

According to the operation principle and key waveform of the primary current, magnetic current, and secondary side current in Figure 4, the magnetic inductance should meet the below requirements:

$$L_m \geq \frac{(V_{Cc}(1-D))^2 T_s}{2 V_O I_O} \tag{41}$$

4. Experimental Results

To verify the correctness of the proposed converter and the above theoretical analysis, a 100 W experimental prototype is built. The specifications and main circuit parameters of the proposed converter are shown in Table 1. The experimental prototype and the experimental platform are presented as in Figures 5 and 6, respectively. The detailed information of the experimental equipment is shown in Table 2.

Table 1. Key Circuit Parameters.

Design Parameter	Value
Input current I_{in}/A	2
Switching frequency f_s/kHz	50
Output current value I_o/A	1
Rated output voltage V_o/V	100
Inductance L_1 and L_2/mH	2
Transformer T turn ratio	2.2
Magnetic inductance L_m/µH	300
Secondary side leakage inductance L_{lk}/µH	1.5
Resonant capacitor C_{r1} and C_{r2}/µF	1
Clamp capacitor C_C/µF	1
Main switches S_1, S_2, S_3, S_4	IRFR220NTRPBF
Schottky diode D_1 and D_2	MBR10200CS
Output filter capacitor C_o/µF	100

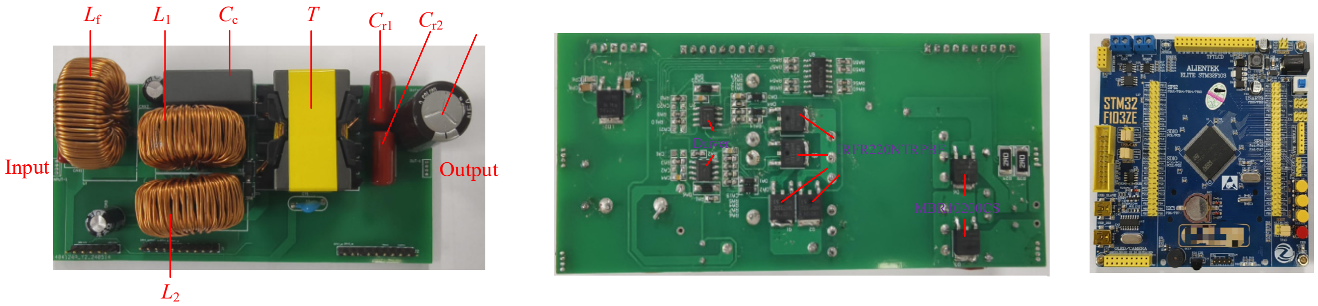

(**a**) (**b**) (**c**)

Figure 5. Experimental prototype. (**a**) Top side of main circuit board; (**b**) Bottom side of main circuit board; (**c**) Control circuit.

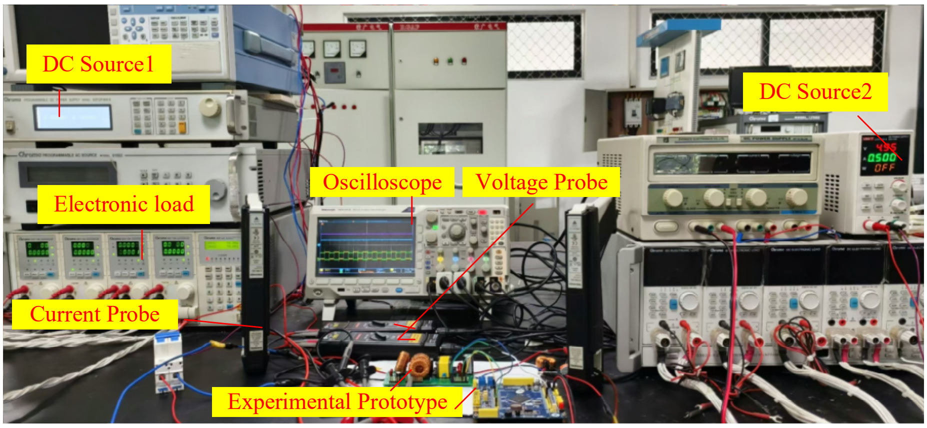

Figure 6. Experimental platform.

Table 2. Experimental equipment setup table.

Equipment Variety	Equipment Model	Function
DC Power Source 1	Chroma 62012P-600-8	Provide input power for the proposed converter.
DC Power Source 2	UNI-TREND UTP1310-II	Provide power supply for the control board.
DC Electronic load	Chroma 6314A + 63115A + 63110A	One channel provides output load for output current source, another channel works with the DC power source 1 to provide the input current source.
Oscilloscope	Tektronix DPO3014	Measure and display waveforms.
Voltage Probe	RIGOL RP1025D	Measure voltage waveforms.
Current Probe	Tektronix TCP0150	Measure current waveforms.
Digital Multimeter	Fluke 17B	Measure input voltage, output voltage, input current, and output current of experimental board.

Figure 7 shows the test waveforms of input current I_{in}, input voltage V_{in}, output current I_o, and output voltage V_o of the proposed converter with 100% load, 80% load, 50% load, and 10% load. From the test waveforms in Figure 8, it can be seen that the converter can convert a 2 A input current to a constant 1 A output current, even if the output voltage varies from 10 V to 100 V.

Figure 8 illustrates test waveforms of the primary voltage v_{TP} of the transformer, primary current i_P of the transformer, secondary current i_S of the transformer, and clamp capacitor voltage v_{Cc} with 100% load and 10% load. From the test waveforms, it can be seen that the clamp capacitor voltages v_{Cc} with 100% load and 10% load are around 110 V and 14 V, respectively, which is the same as the calculation analysis of Equation (24).

Figure 9 shows the experimental waveforms of inductor currents i_{L1} and i_{L2} and driver signals of S_1 and S_2 with 100% load and 10% load. It can be seen that the average current value of i_{L1} and i_{L2} is around 1 A, and the inductor current ripples Δi_{L1} and Δi_{L2} are same because of the same inductor L_1 and L_2 values. The inductor current ripples Δi_{L1} and Δi_{L2} with 100% load and 10% load are around 300 mA and 40 mA, respectively, which is the same as in the theoretical analysis of Equation (34). From the test waveforms of Figures 7–9, the operation waveforms are the same as the theoretical analysis waveforms in Figure 4.

Figure 10 shows the experimental results of the efficiency with different output voltage loads. It can be seen that the conversion efficiency reaches 91.6% with a rated 100 V output voltage load, and the efficiency decreases to 61.5% with a 10 V output voltage load. Compared to the CS/CS converter of references [5,16], the CS/CS converters of [5,16] have no output current regulation control circuit, and thus the constant output current regulation accuracy of the proposed circuit of this paper is better than the circuit in references [5,16]. The deviation of the output current of [5,16] is greater than 8% and 4% when the output voltage changes from 100 V to 10 V, but the output current can be regulated well within the whole output voltage range. The efficiency of the circuit of reference [5] changes from 81% to 52% with the output load voltage variation from 100 V to 20 V; the efficiency of the proposed circuit of this paper changes from 91.6% to 61.5% with the output load voltage variation from 100 V to 10 V. Therefore, compared to the circuits in references [5,16], the output current regulation accuracy and conversion efficiency of the proposed circuit is improved.

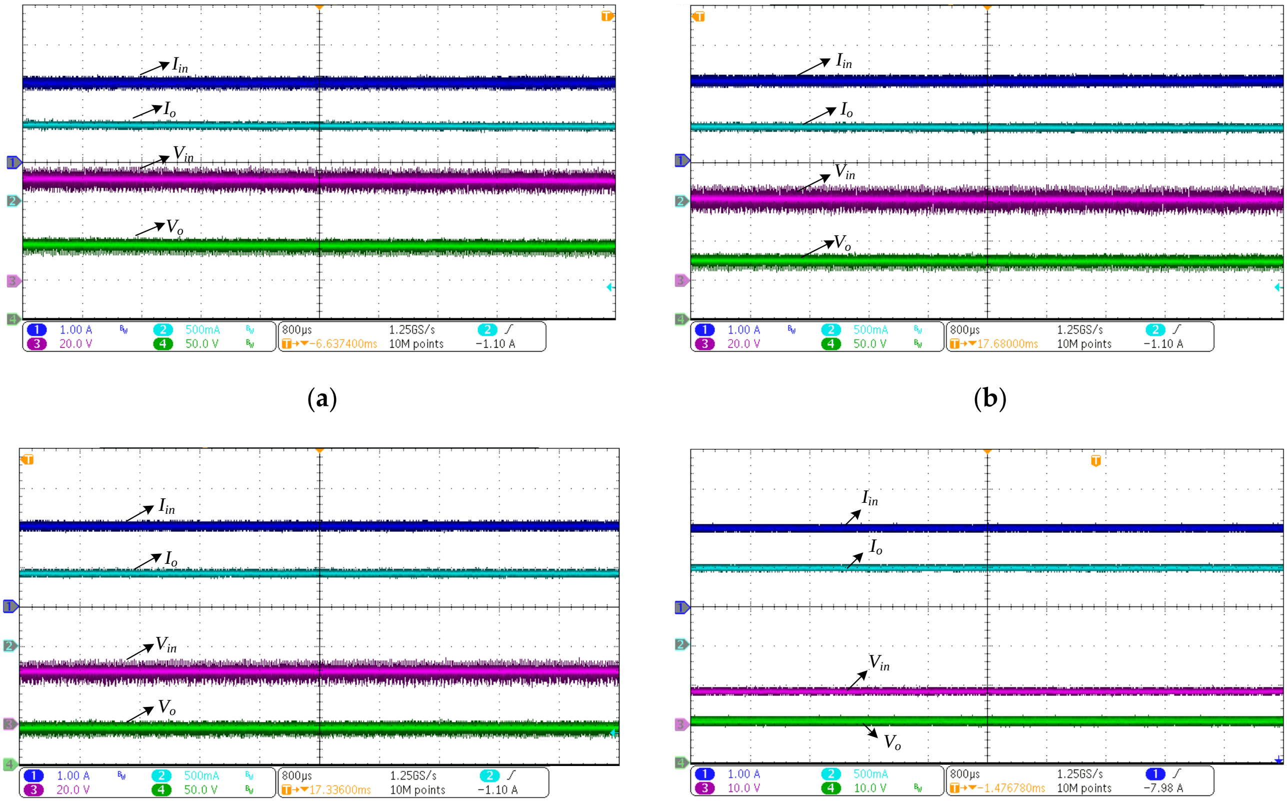

(**a**) (**b**)

(**c**) (**d**)

Figure 7. Test waveforms of input current I_{in}, input voltage V_{in}, output current I_o, and output voltage V_o with different output loads. (**a**) 100% load; (**b**) 80% load; (**c**) 50% load; (**d**) 10% load.

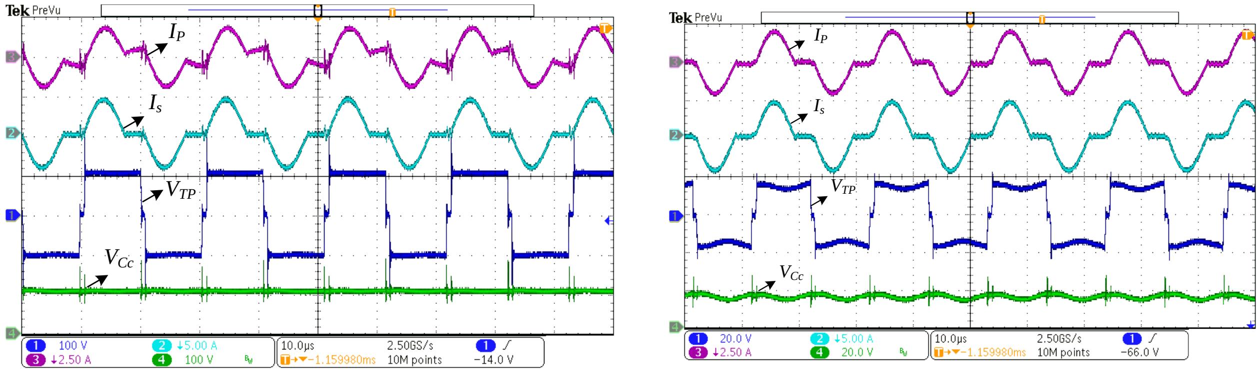

(**a**) (**b**)

Figure 8. Test waveforms of primary voltage v_{TP} of transformer, primary current i_P of transformer, secondary current i_S of transformer, and clamp capacitor voltage v_{Cc} with different loads. (**a**) 100% load; (**b**) 10% load.

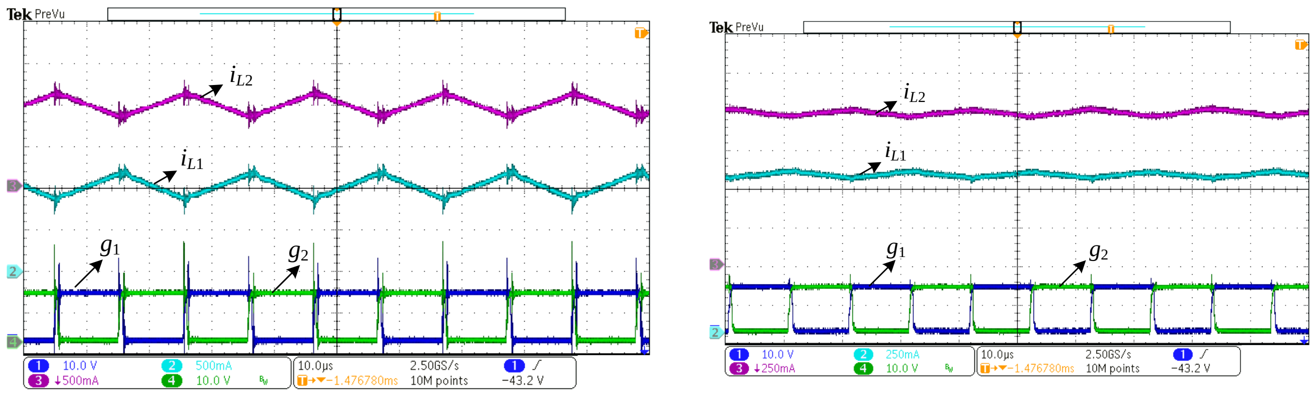

(**a**) (**b**)

Figure 9. Test waveforms of inductor currents i_{L1} and i_{L2} and driver signals of S_1 and S_2 with different output loads. (**a**) 100% load; (**b**) 10% load.

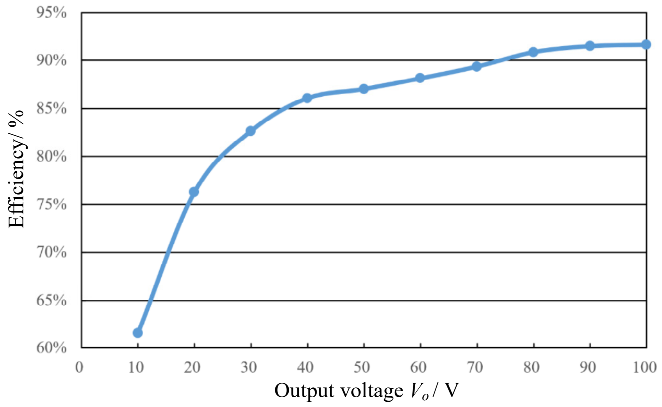

Figure 10. Experimental results of efficiency with different output voltage loads.

5. Conclusions

By employing input current sharing and output voltage doubling circuits, an active clamp dual-inductor isolated CS/CS converter which uses a single-stage conversion circuit to realize constant current source conversion with a wide output voltage range is proposed in this paper. The active clamp circuit at the primary side of the proposed circuit can recover energy stored in leakage inductance, suppress voltage spikes of the primary side switches, and achieve zero-voltage switching of the primary side switches. The secondary side's output voltage doubling circuit helps to achieve a wide range of output volage conversion, and the secondary side's resonant circuit can achieve zero-current switching of the secondary side diodes, which can reduce losses and enhance efficiency. The operating principles and the characteristic and parameter design analysis, including current conversion ratio, transformer turn ratio, power inductors, and resonant capacitors and inductor, are presented. To verify the feasibility of the proposed converter, a 100 W experimental prototype was built and tested. Test results based on the experimental prototype indicated that the proposed converter can achieve current source to current source conversion with a wide output voltage variation rage, and the efficiency can reach 91.6% with a rated load.

Author Contributions: Conceptualization, T.Y. and W.C.; methodology, T.Y., W.C. and D.L.; formal analysis, T.Y., W.C., Y.Z., D.L., J.T. and G.Z.; validation, T.Y., W.C., Y.Z. and D.L.; investigation, T.Y., W.C., Y.Z., J.T. and G.Z.; writing—original draft preparation, T.Y., W.C. and Y.Z.; writing—review and editing, T.Y., W.C., Y.Z., D.L., J.T. and G.Z. All authors have read and agreed to the published version of the manuscript.

Funding: This work was supported by the National Natural Science Foundation of China under Grant No. 62271417, and Chengdu Science and Technology Bureau under Grant No. 2023-JB00-00014-GX and 2024-YF08-00136-GX.

Data Availability Statement: Data of this study is contained within the article. For further inquiries, please contact the corresponding author.

Conflicts of Interest: Author J.T. was employed by the company PowerChina Sichuan Electric Power Engineering Co., Ltd. The remaining authors declare that the research was conducted in the absence of any commercial or financial relationships that could be construed as a potential conflict of interest.

References

1. Yokota, Y.; Matsuda, T. Underwater Communication Using UAVs to Realize High-Speed AUV Deployment. *Remote Sens.* **2021**, *13*, 4173. [CrossRef]
2. Leslie, M.; Pirenne, B.; Qi, D. Developing in the Dark: Software Development and Quality Assurance for the VENUS/NEPTUNE Canada Cabled Observatories. In Proceedings of the OCEANS 2007, Vancouver, BC, Canada, 29 September–4 October 2007; pp. 1–5.
3. Sun, Z.; Wang, Z.; Nie, Z.; Zhao, S.; Yu, Y. Improved GNSS/Acoustic Underwater Positioning with Between-Buoy Baseline Constraint. *J. Surv. Eng.* **2023**, *149*, 04023012. [CrossRef]
4. Asakawa, K.; Muramatsu, J.; Kojima, J.; Shirasaki, Y. Feasibility Study on Power Feeding System for Scientific Cable Network ARENA. In Proceedings of the 2003 International Conference Physics and Control (Cat. No.03EX708), Tokyo, Japan, 25–27 June 2003; pp. 307–312.
5. Asakawa, K.; Kojima, J.; Muramatsu, J.; Takada, T.; Kawaguchi, K.; Mikada, H. Current-to-Current Converter for Scientific Underwater Cable Networks. *IEEE J. Ocean. Eng.* **2007**, *32*, 584–592. [CrossRef]
6. Lu, F.; Zhou, H.; Yue, J.; Peng, X.; He, B.; Wu, Z. Design of an Undersea Power System for the East China Sea Experimental Cabled Seafloor Observatory. In Proceedings of the OCEANS 2013, San Diego, CA, USA, 23–27 September 2013; pp. 1–6.
7. Ma, R.; Wang, R.; Liu, G.; Chen, H.-H.; Qin, Z. UAV-Assisted Data Collection for Ocean Monitoring Networks. *IEEE Netw.* **2020**, *34*, 250–258. [CrossRef]
8. Ak, N.; Demirbas, A. Promising Sources of Energy in the near Future. *Energy Sources Part A Recovery Util. Environ. Eff.* **2016**, *38*, 1730–1738. [CrossRef]
9. Favali, P.; Beranzoli, L. Seafloor Observatory Science: A Review. *Ann. Geophys.* **2021**, *49*, 515–567. [CrossRef]
10. Barnes, C.R.; NEPTUNE Canada Team. Building the World's First Regional Cabled Ocean Observatory (NEPTUNE): Realities, Challenges and Opportunities. In Proceedings of the OCEANS 2007, Vancouver, BC, Canada, 29 September–4 October 2007; pp. 1–8.
11. Asakawa, K.; Muramatsu, J.; Aoyagi, M.; Sasaki, K.; Kawaguchi, K. Feasibility Study on Real-Time Seafloor Glove Monitoring Cable-Network-Power Feeding System. In Proceedings of the 2002 International Symposium on Underwater Technology (Cat. No.02EX556), Tokyo, Japan, 16–19 April 2002; pp. 116–122.
12. Shirasaki, Y.; Yoshida, M.; Nishida, T.; Kawaguchi, K.; Mikada, H.; Asakawa, K. ARENA: A versatile and multidisciplinary scientific submarine cable network of next generation. In Proceedings of the 2003 International Conference Physics and Control. Proceedings (Cat. No.03EX708), Tokyo, Japan, 25–27 June 2003; pp. 226–231.
13. Chen, Y.; Howe, B.M.; Yang, C. Actively Controllable Switching for Tree Topology Seafloor Observation Networks. *IEEE J. Ocean. Eng.* **2015**, *40*, 993–1002. [CrossRef]
14. Glenn, S.; Dickey, T.; Parker, B.; Boicourt, W. Long-Term Real-Time Coastal Ocean Observation Networks. *Oceanography* **2000**, *13*, 24–34. [CrossRef]
15. Zhang, Z.; Xu, F.; Bo, J.; Chen, Y.; Yang, C.; Zhang, F. An Active Node Isolating Method Based on Discrete-Voltage Intervention for Seafloor Observation Network. In Proceedings of the OCEANS 2015, Washington, DC, USA, 19–22 October 2015; pp. 48–59.
16. Asakawa, K.; Kojima, J.; Muramatsu, J.; Takada, T. Novel Current to Current Converter for Mesh-like Scientific Underwater Cable Network-Concept and Preliminary Test Result. In Proceedings of the OCEANS 2003, San Diego, CA, USA, 22–26 September 2003; pp. 1868–1873.
17. Fan, P.; Xu, Y.; Ren, L.; Tang, Y.; Shi, J.; Li, J. Concept Design of BU for Mesh-like Constant Current Seafloor Observation Networks. In Proceedings of the 2021 IEEE 2nd China International Youth Conference on Electrical Engineering (CIYCEE), Chengdu, China, 15–17 December 2021; pp. 1–6.
18. Moradisizkoohi, H.; Elsayad, N.; Mohammed, O.A. A Voltage-Quadrupler Interleaved Bidirectional DC–DC Converter with Intrinsic Equal Current Sharing Characteristic for Electric Vehicles. *IEEE Trans. Ind. Electron.* **2021**, *68*, 1803–1813. [CrossRef]
19. Xuewei, P.; Rathore, A.K. Novel Interleaved Bidirectional Snubberless Soft-Switching Current-Fed Full-Bridge Voltage Doubler for Fuel-Cell Vehicles. *IEEE Trans. Power Electron.* **2013**, *28*, 5535–5546. [CrossRef]
20. Zhou, Y.; Zhou, X.; Zhang, Z. Research on Electric Energy Conversion Methods for Small Power Equipment Based on Constant-Current Power Supply with Submarine Optical Cable. In Proceedings of the 2016 International Conference on Integrated Circuits and Microsystems (ICICM), Chengdu, China, 23–25 November 2016; pp. 306–310.

21. Ninomiya, T.; Higashi, T.; Harada, K.; Tsuya, N.; Gohnai, T.; Honda, Y. Analysis of the Static and Dynamic Characteristics of Push-Pull Parallel Resonant Converters. In Proceedings of the 17th Annual IEEE Power Electronics Specialists Conference, Vancouver, BC, Canada, 23–27 June 1986; pp. 367–374.
22. Saha, T.; Wang, H.; Riar, B.; Zane, R. Analysis and Design of a Parallel Resonant Converter for Constant Current Input to Constant Voltage Output DC-DC Converter Over Wide Load Range. In Proceedings of the 2018 International Power Electronics Conference (IPEC-Niigata 2018-ECCE Asia), Niigata, Japan, 20–24 May 2018; pp. 4074–4079.
23. Modepalli, K.; Mohammadpour, A.; Li, T.; Parsa, L. Three-Phase Current-Fed Isolated DC–DC Converter with Zero-Current Switching. *IEEE Trans. Ind. Appl.* **2017**, *53*, 242–250. [CrossRef]
24. Zhang, Z.; Zhou, X.; Wang, X.; Wu, T. Design, Analysis, and Modeling of an Isolated Constant-Current to Constant-Voltage Converter in Cabled Underwater Information Networks. *Electronics* **2019**, *8*, 961. [CrossRef]
25. Wang, L.; Wang, X.; Zhou, X.; Chen, S. Design and Analysis of an Isolated Constant Current to Constant Current Converter with Capacitor Transferring Energy. In Proceedings of the 2020 IEEE 1st China International Youth Conference on Electrical Engineering (CIYCEE), Wuhan, China, 1–4 November 2020; pp. 1–7.

Disclaimer/Publisher's Note: The statements, opinions and data contained in all publications are solely those of the individual author(s) and contributor(s) and not of MDPI and/or the editor(s). MDPI and/or the editor(s) disclaim responsibility for any injury to people or property resulting from any ideas, methods, instructions or products referred to in the content.